Effect of phosphoric acid as slurry additive on $Li_4Ti_5O_{12}$ lithium-ion anodes

Yun Xu [a,b], Angelo Mullaliu [a,b], Shawn D. Lin [c], Yanjiao Ma [a,b], Jakob Asenbauer [a,b], Maider Zarrabeitia [a,b], Stefano Passerini [a,b], Dominic Bresser [a,b,*]

[a] Helmholtz Institute Ulm (HIU), Helmholtzstrasse 11, Ulm 89081 Germany
[b] Karlsruhe Institute of Technology (KIT), P.O. Box 3640, Karlsruhe 76021, Germany
[c] National Taiwan University of Science and Technology (NTUST), Keelung Road 43 s. 4, Taipei 106, Taiwan

ARTICLE INFO

Keywords:
$Li_4Ti_5O_{12}$
Aqueous processing
Phosphoric acid
Anode
Lithium-ion battery

ABSTRACT

The aqueous processing of lithium-containing electrode materials is challenged by the reactivity of such materials towards water, resulting in lithium leaching, slurry pH increase, and consequent corrosion of the aluminum current collector. The addition of (mild) acids to the aqueous electrode slurry has been reported as a viable method to suppress the corrosion issue. Herein, we present a comprehensive investigation of the addition of phosphoric acid (PA) to an aqueous electrode slurry containing $Li_4Ti_5O_{12}$ as the active material. Following an initial evaluation of the slurry pH evolution as a function of the PA content, a comparative investigation of the PA-free electrodes and the "corrosion-free" electrodes was performed. The latter clearly outperform the PA-free electrodes in terms of their electrochemical performance. Interestingly, this is not only resulting from the buffered pH, but the phosphate anion also plays a decisive role.

1. Introduction

Lithium-ion batteries (LIBs) are the electrochemical energy storage technology of choice for a variety of applications, including small portable electronic devices, (hybrid) electric vehicles, and stationary energy storage [1]. The great majority of these LIBs comprise graphite as the active material for the negative electrode, but a significant share contains $Li_4Ti_5O_{12}$ (LTO) owing to its exceptional cycle life, superior safety, and potentially faster charging [1–7]. While such properties are somehow intrinsic to the active material, the design, composition, and fabrication of the eventual electrode are at least as important [8]. These include the choice of the binding agent, which also has a great environmental impact – not only with regard to the binding agent itself, but also the processing solvent. Water-based binders are clearly favored over binders that require the use of harmful *N*-methyl-2-pyrrolidone (NMP) [9]. Therefore, tremendous efforts have been devoted to the optimization of advanced binding agents for LTO-based electrodes [10–14], as well as LIB electrodes in general [9]. The general compatibility of LTO with water-soluble binder has been reported by Fongy et al. [15] in 2012, revealing that no major degradation of the active material occurred in contact with water. Nonetheless, just like other lithium transition metal oxides also LTO suffers lithium leaching when being dispersed in water. This leads to LiOH formation, an increase of the slurry's pH value, and, eventually, pitting corrosion of the aluminum current collector [13], accompanied by severe cracking of the electrode coating layers [16]. The latter issue results in poor adhesion of the coating layer to the aluminum current collector and a large charge transfer resistance that decreases the rate performance [17]. The underlying reaction with water appears to be rather fast when the material is simply exposed to water, as indicated by a rather rapidly stabilizing pH value above 11 [18]. This increase of the pH value was addressed in a previous study [13] by adding phosphoric acid (PA) to the electrode slurry, which buffers the pH value and, thus, suppresses the pitting corrosion of the aluminum current collector. This latter phenomenon is also accompanied by hydrogen evolution leading to large crater-like holes in the electrode coating. While this approach was successfully employed also for the aqueous processing of $Li[Ni_{0.33}Mn_{0.33}Co_{0.33}]O_2$ (NMC_{111}) [19], $Li[Ni_{0.5}Mn_{0.3}Co_{0.2}]O_2$ (NMC_{532}) [20], $Li[Ni_{0.8}Mn_{0.1}Co_{0.1}]O_2$ (NMC_{811}) [21], $LiNi_{0.5}Mn_{1.5}O_4$ (LNMO) [22–25], and lithium-rich $Li_{1.2}Ni_{0.16}Mn_{0.56}Co_{0.08}O_2$ (LR-NMC) [26], revealing the formation of a metal phosphate surface layer on these positive electrode active materials, the investigation of LTO in combination with PA remained limited to the determination of the adhesion strength and the evaluation in LTO||NMC_{111} full-cells [13].

Herein, an in-depth investigation of the impact of adding PA to LTO-based electrode slurries is presented. Following an analysis of the pH

* Corresponding author at: Helmholtz Institute Ulm (HIU), Helmholtzstrasse 11, Ulm 89081 Germany.
E-mail address: dominic.bresser@kit.edu (D. Bresser).

evolution as a function of milling time and PA content, a comparative study of the electrochemical behavior of the resulting LTO-based electrodes combined with *ex situ* scanning electron microscopy (SEM) reveals a superior performance of the electrodes to which PA was added. Interestingly, new rod-shaped particles were formed in such case, which were not observed in the earlier studies for NMC, LNMO, and LR-NMC.

2. Experimental

2.1. Electrode preparation

The electrodes were composed of 88 wt% LTO (NEI Corporation), 5 wt% of conductive carbon (Super C45, IMERYS), and 7 wt% sodium carboxymethyl cellulose (CMC, Dow Wolff Cellulosics). The slurry was prepared as follows. CMC was dissolved in deionized water *via* magnetic stirring at room temperature. Subsequently, a selected amount of PA (>99%, Bernd Kraft; 33% aqueous solution) was added – except for the PA-free reference electrode. The PA content was varied from 0.67 wt% (1PA), over 1.34 wt% (2PA), and 2.01 wt% (3PA) to 2.68 wt% (4PA) versus the mass of LTO in the slurry. In the next step, the conductive carbon and LTO were added to the aqueous dispersion. The resulting slurry was dispersed by planetary ball milling (Fritsch Vario PULVERISETTE 4) for 2 h at 1100 rpm and then cast on battery-grade aluminum foil using a laboratory-scale doctor blade with a wet film thickness of 200 μm. After immediate pre-drying in an atmospheric oven (ED-115, Binder) at 80 °C, disk-shaped electrodes (geometric area: 1.13 cm^2) were punched and dried at room temperature overnight in the dry room. Finally, the electrodes were further dried under vacuum at 120 °C for 12 h and pressed at 5 tons for 10 s (Atlas manual hydraulic press, Specac). The active material mass loading of the disk electrodes ranged from 5.3 to 5.8 mg cm^{-2}. The residual moisture in the dried 0PA and 4PA electrodes was measured in argon atmosphere using a Coulometric KF Titrator (C30, METTLER TOLEDO) and about 0.2 g of each sample, revealing a water content of about 300 and 500 ppm in the case of the 4PA and 0 PA electrodes, respectively. The porosity ε of the electrodes was calculated based on the mass loading L and thickness m of the electrode coating. ρ represents the density of the different electrode components, while $x_{AM}, x_{CB}, and\ x_B$ represent the mass ratio of the active material (AM), carbon black (CB), and binder (B) in the electrode.

$$\varepsilon = 1 \quad \frac{m}{L}\left(\frac{x_{AM}}{\rho_{AM}} + \frac{x_{CB}}{\rho_{CB}} + \frac{x_B}{\rho_B}\right)$$

The calculations revealed an average porosity of about 50% and 55% for the 4PA and 0PA electrodes, respectively, i.e. rather similar values – especially when considering the morphology of the 0PA-type electrodes. The adhesion strength of the electrode coating layer to the current collector was determined using a zwickiLine device (2.5 KN, ZwickRoell) and electrode samples with an area of 6.45 cm^2. The experiment was repeated at least 5 times each. The pH measurements during the electrode slurry dispersion were conducted every 30 min at 21 ± 2 °C, using a Lab 860 pH meter (SI Analytics) with a Blue Line 18 pH electrode (Schott Instruments).

2.2. Physicochemical characterization

Scanning electron microscopy (SEM) was performed using a Zeiss Crossbeam 340 field-emission scanning electron microscope, equipped with a Capella focused ion-beam (FIB, gallium ion source) and an energy dispersive X-ray (EDX) spectrometer (Oxford Instruments X-Max Xtreme, 100 mm^2, 1 5 kV). A single reflection, diamond attenuated total reflection (ATR) accessory PLATINUM ATR from Bruker was utilized for the ATR infrared (ATR-IR) spectroscopy analysis. The spectrum obtained for the 4PA-type electrodes was background-corrected *via* the spectrum recorded for the 0PA-type electrodes. X-ray photoelectron spectroscopy (XPS) was carried out using a monochromatic Al K_α (hν = 1486.6 eV) X-ray source and a Phoibos 150 XPS spectrometer, equipped with a microchannel plate and a delay line detector (DLD). High resolution scans were obtained with an X-ray source power of 200 W, 20 eV pass energy, and 0.1 eV energy steps in fixed analyzer transmission mode. The photoelectron data were calibrated versus the graphitic C=C (sp^2) peak at 284.4 eV originating from the presence of the conductive carbon in the electrodes. The fitting of the spectra was performed with the CasaXPS software, employing a nonlinear Shirley-type background and a 30% Lorentzian and 70% Gaussian profile function. Inductively coupled plasma optical emission spectrometry (ICP-OES) was conducted on a Spectro Arcos spectrometer (Spectro Analytical Instruments) to investigate the lithium and titanium leaching. For these measurements, 0.44 g of LTO powder were dispersed in deionized water (in the presence or absence of PA) by ball milling for 2 h analogously to the slurry preparation. Subsequently, the dispersions were centrifuged and the liquid phase was analyzed *via* ICP-OES. X-ray diffraction (XRD) was performed using a Bruker D8 Advance (Cu K_α radiation, $\lambda = 0.15406$ nm). The 2θ range was set to $5° \leq 2\theta \leq 70°$ and the step size was 0.008° (2θ) with an acquisition time of 1 s per point. Rietveld refinement was conducted utilizing the GSAS-II software [27], assuming the structural model reported by Jovic et al. [28,29]. The instrumental parameters were obtained from a LaB_6 standard; accordingly, the instrumental broadening parameters, *i.e.*, U, V, W, X, and Y, were kept fixed to $4.397\bullet10^{-4}$ deg^2, $-5.720\bullet10^{-4}$ deg^2, $2.577\bullet10^{-4}$ deg^2, $1.855\bullet10^{-2}$ deg, and $2\bullet10^{-5}$ deg, respectively. The scale factor, background, sample displacement, unit cell parameters, peak shape, and atomic parameters were refined in the given order.

2.3. Electrochemical characterization

For the electrochemical characterization, coin cells (CR2032, Hohsen) were used if not indicated differently. In the case of the half-cell tests, lithium metal foil (battery grade, Honjo) served as the counter electrode. The cell assembly was carried out in an argon-filled glovebox (MBraun) with a H_2O and O_2 content lower than 0.1 ppm. A polyethylene separator (Asahi Kasei, Hipore SV718) was used soaked with 100 μL of the electrolyte solution (1 M $LiPF_6$ in ethyl carbonate (EC)/dimethyl carbonate (DMC), 1:1 w/w, UBE). After assembly, the cells were left to rest for 6 h to ensure a homogeneous wetting of the electrodes with the electrolyte. Galvanostatic cycling was performed at 20 ± 2 °C using a Maccor Battery Tester 4300. The cut-off voltages were set to 1.0 V and 2.5 V. All voltage values for the tests with coin cells refer to the lithium metal counter electrode. The dis-/charge rate of 1C corresponds to the specific current of 170 mA g^{-1}. Cyclic voltammetry (CV) experiments were conducted on a multichannel potentiostat (VMP3, BioLogic), using three-electrode Swagelok-type T-cells with lithium metal as the counter and reference electrodes. The sweep rate was 0.1 mV s^{-1} and the cut-off potentials were set to 1.2 and 3.5 V. In this case, the given potential values refer to the lithium metal quasi-reference electrode. Electrochemical impedance spectroscopy (EIS) was performed utilizing three-electrode ECC-PAT-Core cells (EL-CELL) with lithium foil as the counter electrode and lithium metal ring as the reference electrode. The applied AC signal had an amplitude of 5 mV and the frequency ranged from 1 MHz to 10 mHz.

3. Results and discussion

The evolution of the pH value as a function of time for the aqueous LTO dispersions in absence of PA (0PA) or in presence of varying amounts of PA (1PA, 2PA, 3PA, and 4PA) during ball milling is depicted in Fig. 1a. In all cases, the pH value increased with time as a result of the continuous lithium leaching. In the absence of PA, the pH value was by far the highest at the beginning with almost 11 (10.9) and maintained to be the highest throughout the ball milling process, leveling off at 12.1 after 1.5 h. When adding PA, the initial pH value was well below 6 for 1PA, close to 5 for 2PA, and lower than 5 for 3PA and 4PA. After ball

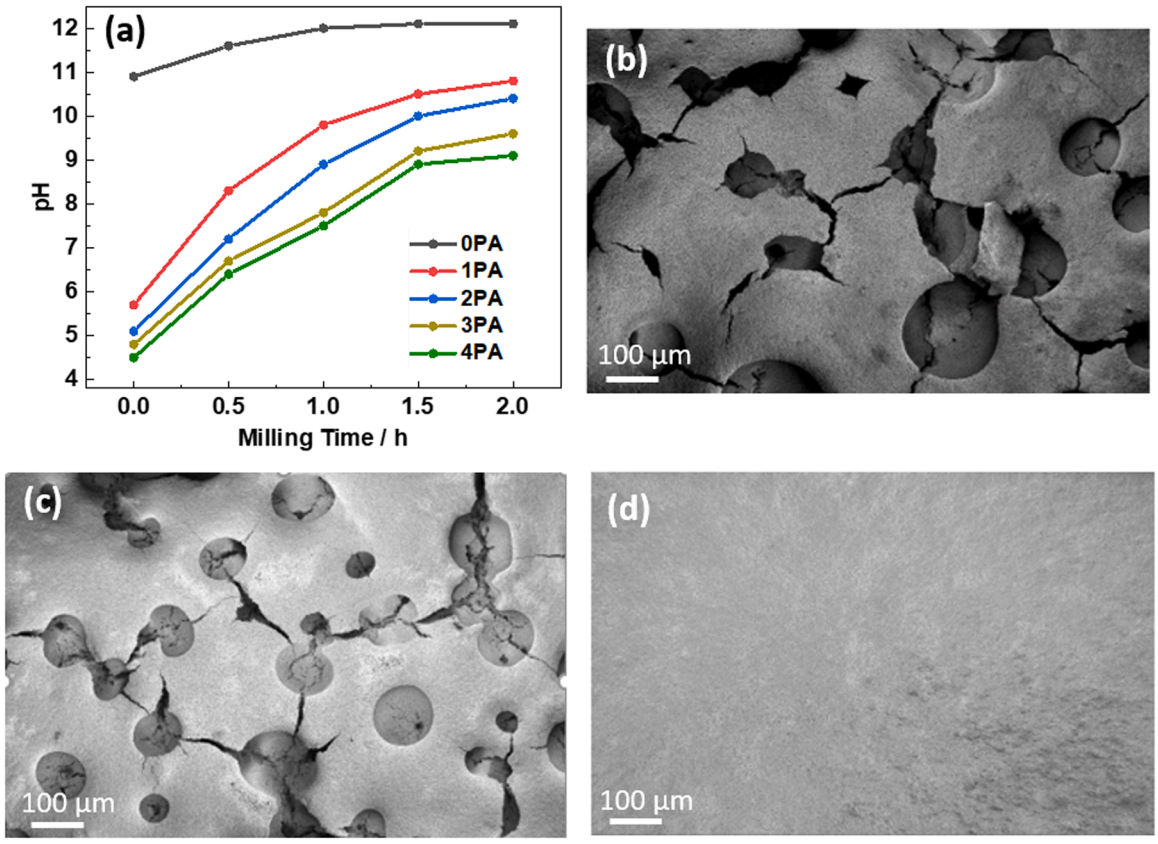

Fig. 1. (a) Evolution of the pH value of aqueous LTO slurries in absence of PA (0PA) or in presence of varying amounts of PA (1PA, 2PA, 3PA, and 4PA) as a function of time during ball milling. (b–d) SEM micrographs of pristine LTO-based electrodes prepared (b) without adding PA (0PA), and with (c) 1PA and (d) 4PA.

milling for 2 h, however, the pH increased substantially to 10.8, 10.4, 9.6, and 9.1 for, respectively, 1PA, 2PA, 3PA, and 4PA. The pH value of the latter slurry is considered to be at the borderline of the corrosion regime of aluminum, while all former values are within the corrosion regime [19,22].

The SEM images of the corresponding electrodes are in good agreement with these findings. The 0PA electrode (Fig.1b) shows extensive crater-like holes with a diameter exceeding 100 µm resulting from the aluminum corrosion induced hydrogen evolution, which are interconnected by severe cracks [22]. Going to the 1PA electrode (Fig. 1c), the crater-like holes appear slightly smaller and the cracking is less severe, resulting from the lower pH value. In the case of 4PA (Fig. 1d), however, the corrosion appears successfully prevented in line with the significantly lower pH value. Accordingly, these two electrodes (0PA and 4PA), as the "end members" with regard to the pH value, were selected for the forthcoming in-depth investigation of the impact of adding PA to the electrode slurry.

Prior to the electrochemical characterization, we evaluated the impact of the corrosion and crater-like holes on the adhesion strength of the electrode coating layer to the aluminum current collector. Both the tensile force and tensile stress were significantly higher for the 4PA electrodes compared to the 0PA electrodes with ca. 750 N and 1.2 N mm ^{2} vs. ca. 640 N and 1.0 N mm ^{2}, respectively. Interesting to note in this regard is that the in the case of the 0PA electrodes, the breaking point appears to be within the electrode coating layer. This might be related to the hydrogen evolution owing to the aluminum corrosion and the resulting weakening of the cohesion of the electrode components – to a certain extent also indicated by a slightly higher porosity.

Subsequently, these two kinds of electrodes were subjected to galvanostatic cycling at varying C rates (Fig. 2). At lower C rates of 0.1C to 0.5C, no significant difference in specific capacity is observed (Fig. 2a, b). The capacity at 0.1C, for instance, is about 165 mAh g ^{1} for both the electrodes, i.e., fairly close to the theoretical maximum of 175 mAh g ^{1}. Starting from 1C, however, the specific capacity of the 4PA electrodes becomes increasingly higher. For example, the latter electrodes deliver 114, 91, and 69 mAh g ^{1} at 4C, 7C, and 10C, respectively, while the 0PA electrodes achieve only 83, 37, and 16 mAh g ^{1}. Additionally, the cycling stability after 200 galvanostatic cycles at 1C is lower for the 0PA electrodes (120 mAh g ^{1}) than for the 4PA electrodes (142 mAh g ^{1}) (Fig. 2a). Comparing these capacity values with those recorded during the 20th cycle at 1C, i.e., 145 mAh g ^{1} for 0PA and 150 mAh g ^{1} for 4PA, capacity retention of, respectively, 82.8% and 94.7% are obtained once more highlighting the superior performance of the 4PA electrodes.

The comparison of the voltage profiles at the different C rates (Fig. 2 c,d) shows as the superior rate capability of the 4PA electrodes originates from a substantially lower polarization ΔE at elevated C rates (see also Fig. 2e for the direct comparison). At 2C, for instance, ΔE amounts to about 280 mV for the 0PA electrodes, while it is only 167 mV in the case of 4PA. At 7C it is around 330 mV for 4PA and almost three times as high for 0PA with more than 900 mV. In fact, a comparative EIS analysis shows that the cell resistance with the 0PA electrodes (66 Ω) is higher than of those with the 4PA electrodes (47 Ω) already in the pristine state (Fig. S1). Generally, these results show that the addition of PA and the consequent suppression of the aluminum corrosion is essential for obtaining good rate capability and cycling stability. It might be noted that the extensive polarization in the case of 0PA is not only detrimental to the performance, but has an important impact on the energy efficiency, as any polarization leads to a significant loss in the form of heat [30]. The inferior rate capability and cycling stability of 0PA electrodes is also evidenced during the further constant current cycling at 4C (Fig. 2f). After an initial decrease in both cases, the specific capacity stabilizes at about 120 mAh g ^{1} for 4PA, which is well maintained also after 200 cycles, while it steadily decreases from about 90 mAh g ^{1} at the 10th cycle to about 70 mAh g ^{1} after 200 cycles for 0PA.

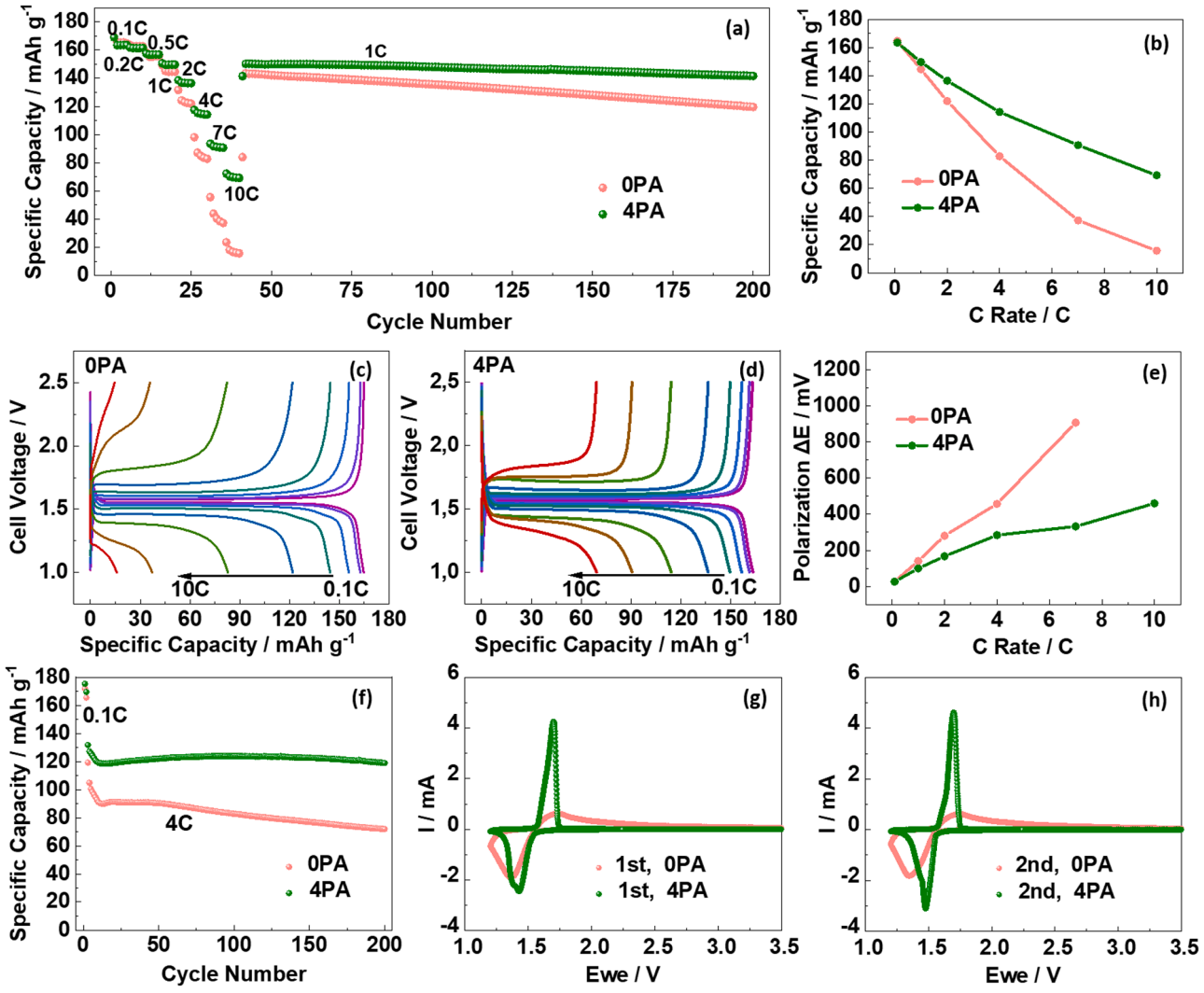

Fig. 2. Electrochemical characterization of 0PA-type and 4PA-type LTO electrodes with lithium metal counter electrodes: (a–e) Galvanostatic cycling at varying C rates with 5 cycles at each C rate, i.e., 0.1C, 0.2C, 0.5C, 1C, 2C, 4C, 7C, and 10C, followed by 160 cycles at 1C (cut-off voltages: 1.0 V and 2.5 V), with (a) the plot of the specific charge capacity vs. the cycle number, (b) the plot of the specific capacity vs. the C rate (always for the 5th cycle at each C rate), (c,d) the plot of the corresponding dis-/charge profiles for (c) 0PA and (d) 4PA, and (e) the plot of the polarization ΔE vs. the C rate (ΔE is defined as the difference between two voltage plateaus). (f) Galvanostatic cycling at a constant C rate of 4C for 200 cycles after two initial cycles at 0.1C. (g,h) Cyclic voltammetry experiments with panel (g) showing the comparison of the first cyclic sweep and (h) the second cyclic sweep.

It is worth noting that the rate capability of the 4PA electrodes (see Fig. 2a) is superior to a previous study on micrometer-sized LTO particles [2] despite the higher mass loading used herein. To further investigate this different behavior, the electrodes were subjected to CV experiments (Fig. 2 g,h). Fig. 2g shows the comparison of the first cyclic sweep. Both cells reveal the characteristic redox peak couple associated with the reversible phase transition from spinel $Li_4Ti_5O_{12}$ to rock-salt $Li_7Ti_5O_{12}$ upon lithium insertion [31–33]. The current intensity, however, is clearly higher for 4PA, while the peak separation is smaller, indicating favourable de-/lithiation kinetics and higher reversibility. For 0PA, the maximum of the cathodic peak (φ_c) is located at around 1.37 V and the anodic peak (φ_a) shows its maximum at 1.73 V, resulting in a peak separation $\Delta\varphi$ (φ_a-φ_c) of 360 mV. In the case of 4PA, the φ_a is 1.69 V and φ_c is 1.42 V, leading to a peak separation $\Delta\varphi$ of 270 mV, which is substantially smaller than for 0PA. In the second cyclic sweep, $\Delta\varphi$ increases for 0PA to 410 mV, while it decreases for 4PA to about 230 mV, i.e., roughly half the value. This difference in peak separation is in good agreement with the greater polarization observed for 0PA during the galvanostatic experiments and underlines the beneficial impact of adding PA to the electrode slurry.

One reason might be the slightly reduced lithium leaching when PA is present in the slurry, 0.71 mg (0PA) versus 0.63 mg (4PA) were determined by ICP-OES analysis of the slurry's liquid phase, in line with previous studies on other lithium-containing active materials [20,34]. The loss of lithium at the particle surface might especially have a negative impact on the charge transfer at the particle|electrolyte interface [35]. Another reason might be the extensive film formation on the 0PA electrode upon cycling as highlighted by *ex situ* SEM (Fig. 3a and S2). These certainly add to the polarization, charge transfer resistance, and capacity fading. In the case of 4PA, such a surface film and particle cracking are not observed (Fig. 3b). Instead, the *ex situ* SEM analysis of the cycled 4PA electrodes reveals another rather surprising finding: relatively large rod-shaped particles with a diameter in the sub-micrometer range and length of several micrometers (Fig. 3c). Such particle shape is not observed for the pristine LTO powder (Fig. S3), neither for the cycled 0PA electrodes.

Accordingly, a more careful evaluation of pristine (Fig. 4) and cycled (Fig. 5) 4PA electrodes *via* SEM coupled with EDX mapping was performed, showing that a relatively large number of such rod-shaped particles, which appear to be of rather high crystallinity with regard

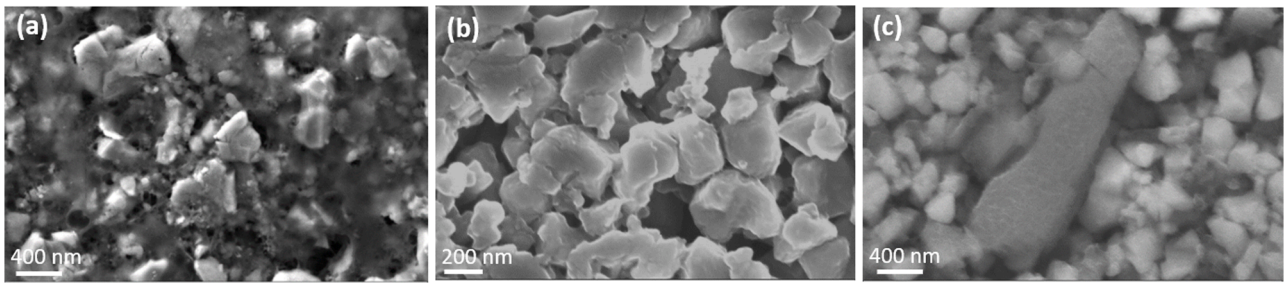

Fig. 3. *Ex situ* SEM micrographs of cycled LTO electrodes: (a) 0PA at a magnification of 30kx; (b,c) 4PA at a magnification of (b) 50kx and (c) 30kx (for the cycling procedure, see Fig. 2**a**).

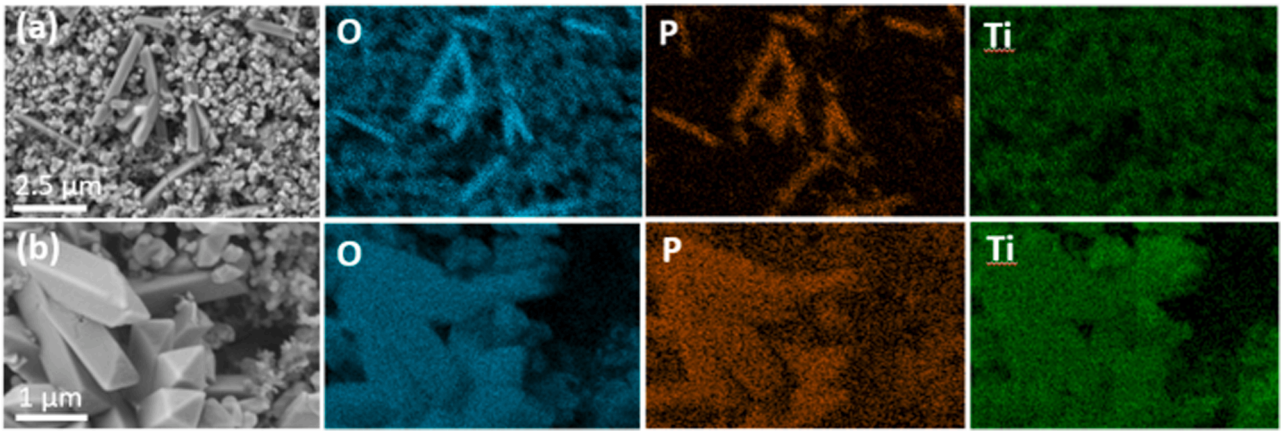

Fig. 4. SEM/EDX analysis of pristine 4PA-type LTO electrodes at a (a) lower and (b) higher magnification with a mapping of oxygen, phosphorus, and titanium (from left to right).

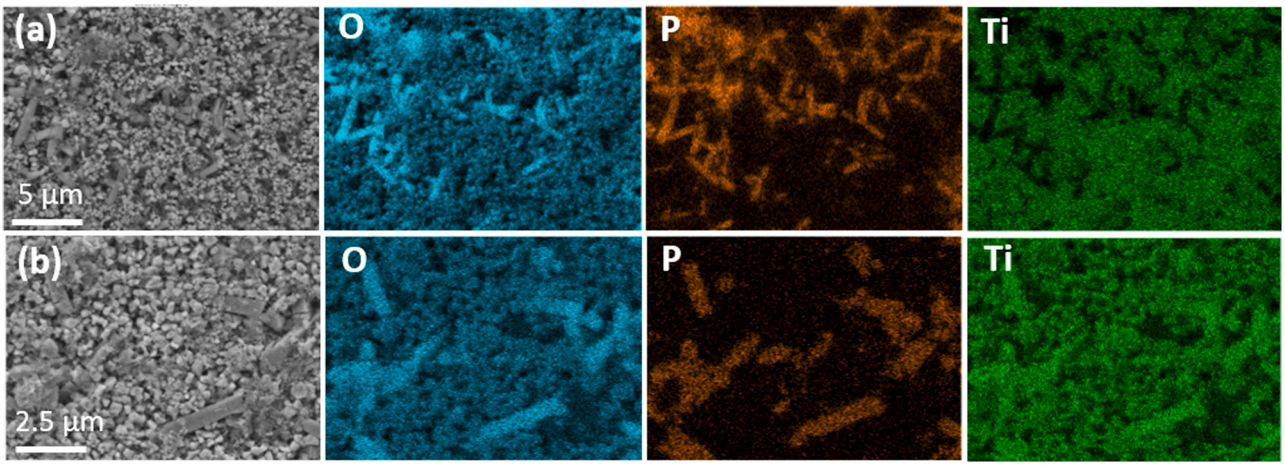

Fig. 5. SEM/EDX analysis of cycled 4PA-type LTO electrodes (see Fig. 2**a** for the cycling procedure) at a (a) lower and (b) higher magnification with a mapping of oxygen, phosphorus, and titanium (from left to right).

to the clear edges and tips (Fig. 4b), is present. Moreover, phosphorus is essentially concentrated in these rod-shaped particles. The comparison of the P and Ti distribution also reveals a large overlap of the two elements (in addition to oxygen). However, the P and Ti overlap is not perfect, meaning that some of the P-containing particles do not show a significant concentration of titanium. This is particularly apparent in Fig. 5a in the upper left corner, for instance.

Given the information provided by SEM/EDX we may assume that the formation of the large rod-shaped particles is a general phenomenon for the 4PA electrodes. To further investigate the nature of these rod-shaped particles forming upon electrode preparation when PA is added into the slurry, a comprehensive characterization of the pristine electrodes *via* XRD (Fig. 6), XPS (Fig. 7), and ATR-IR (Fig. 8) was conducted. The refined XRD pattern of the pristine LTO powder is presented in **Fig. S4** and the retrieved lattice parameter, atomic distances, and positions are provided in **Table S1**. The analysis shows a phase-pure spinel-structure material. The comparison of the XRD patterns recorded for the 0PA and the 4PA electrodes (Fig. 6 a,b) with the XRD pattern recorded for the pristine material (Figs. S4 and 6b) reveals three additional very broad reflections for the 0PA electrode at about 28.3°, 30.2°, and 31.5° (marked by asterisks), which are matching fairly well, for instance, with the PDF references no. 01–075–4926 (28.3°) and

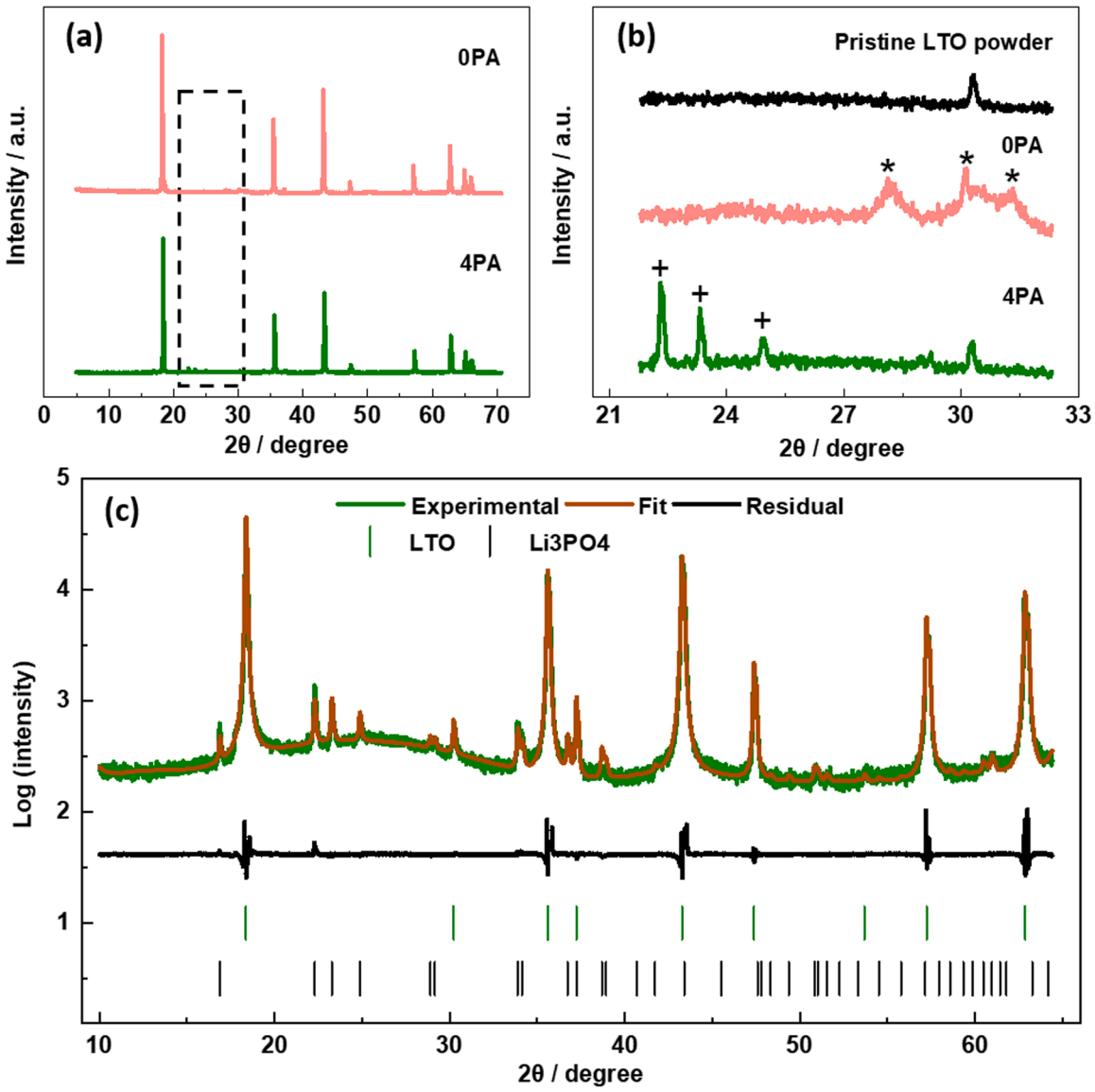

Fig. 6. (a) Comparison of the XRD patterns recorded for the pristine 0PA- and 4PA-type electrodes. (b) Magnification of the 2θ region from 21° to 33°, as highlighted in (a). (c) Result of the Rietveld refinement of the XRD pattern recorded for the 4PA-type electrode (the intensity is plotted in the log scale to increase the visibility of the Li_3PO_4-related reflections).

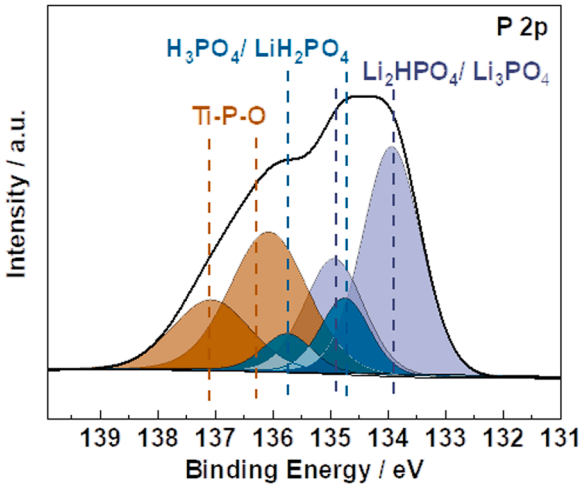

Fig. 7. XPS P 2p photoelectron region for the pristine 4PA-type LTO electrodes.

00–023–1009 (31.5°) for AlO(OH) and Al_2O_3, respectively, suggesting that these are related to aluminum corrosion products [36]. These corrosion-related reflections are absent for the 4PA electrodes, which is in good agreement with the absence of corrosion-related craters in the electrode coating (Fig. 1). However, instead four additional, low-intensity reflections at 16.9°, 22.3°, 23.3°, and 24.9° 2θ angles were observed in the case of 4PA (see Fig. 6b for the magnification; the additional reflections are marked by crosses). These additional reflections are matching well with the PDF reference no. 01–084–0003 for Li_3PO_4. The Rietveld refinement of the XRD pattern obtained for the 4PA electrodes is presented in Fig. 6c and the retrieved lattice parameter, atomic distances, and positions are provided in Table S2; the latter are not considering the presence of the Li_3PO_4-related reflections. Generally, the results are in good agreement with the structural model for cubic (space group: *Fd*-3 m) LTO [29], indicating that the bulk LTO phase was not affected by the addition of PA. The refinement also shows that there is an appreciable amount of Li_3PO_4 formed. This suggests that the reduced amount of lithium in the liquid phase detected by the ICP-OES analysis results from the lithium "trapping" within the poorly water-soluble, solid Li_3PO_4 phase. Moreover, the rather large amount of

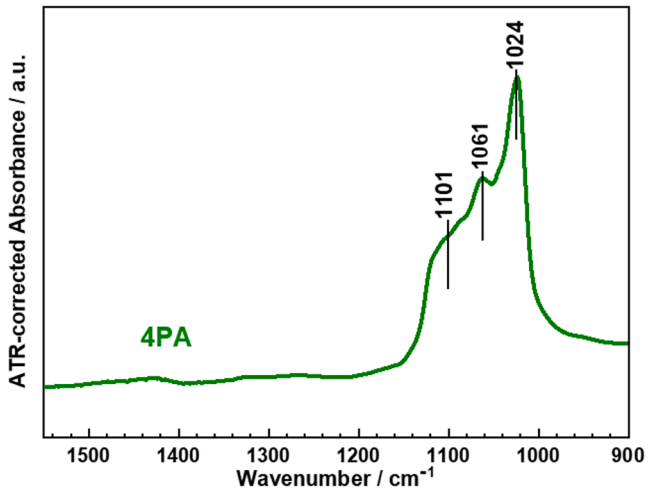

Fig. 8. ATR-IR spectrum of pristine 4PA-type LTO electrodes with an indication of the bands assigned to the lithium titanium phosphate phase.

lithium phosphate formed suggests that the addition of PA favors, in fact, lithium dissolution from the LTO phase to a certain extent. Nonetheless, the specific capacity remains essentially unaffected at low C rates. The first cycle Coulombic efficiency of the 4PA electrode (97%) is slightly lower than that of the 0PA (99%), which may result from the electrochemical "re-lithiation" to a certain extent.

The XPS analysis of the 4PA electrodes in the P 2p region further corroborates the presence of Li_3PO_4 (Fig. 7). However, the fitting also suggests the presence of mixed Li_xH_yPO4 (with $x + y \approx 3$) phases, with the "lithium-rich" phosphate phase showing slightly lower binding energies (Li_2HPO_4/Li_3PO_4; P $2p_{3/2}$: 133.8 eV) and the "lithium-poor" phase showing higher binding energies (H_3PO_4/LiH_2PO_4; P $2p_{3/2}$: 134.6 eV) [22,37,38]. Additionally, the XPS data indicate the presence of a titanium-containing phosphate phase (Ti-P-O; P $2p_{3/2}$: 136.1 eV), which is in agreement with the SEM/EDX data (Figs 4 and 5). The absence of any related reflections in the XRD pattern suggests that this phase is mostly amorphous or present only in small amounts at the surface and, thus, not detectable by XRD.

ATR-IR analysis of 4PA (Fig. 8) clearly revealed a broad band with several peaks at 1101, 1061, and 1024 cm^{-1} when using 0PA as the reference. This suggests the presence of overlapping P-O vibration bands and it is in fairly good agreement with the previously reported range of P-O vibration of lithium titanium phosphate [39]. It is interesting to note that lithium titanium phosphate with a rhombohedral or orthorhombic structure and also α-$TiPO_4$ have been reported earlier as potential electrode active material with a specific capacity of up to about 120 mAh g^{-1} [40–42]. The (lithium) titanium phosphate formed herein, however, appears to be electrochemically inactive, as the CV data (Fig. 2g,h) do not show any redox feature in the expected potential range from 1 to 3 V [40–42], which might be related to its amorphous nature. The impact of the presence of this phase (if any – apart from the trapping of lithium and titanium during the electrode preparation and the resulting pH buffering effect) needs to be further understood – just like the presence of Li_3PO_4. The incorporation of the latter into the electrode has been shown to be advantageous already for the electrochemical performance of several active materials, including LNMO [43], $LiFePO_4$ [44], Li_2FeSiO_4 [45], Bi [46], and also LTO/TiO_2 composite microelectrodes [47], and assigned to its good ionic conductivity and enhanced charge transport kinetics. While a detailed understanding of the beneficial impact is still missing, to the best of our knowledge, the results reported herein (and in the aforementioned previous studies) and the finding that this phase is formed during the aqueous electrode preparation of lithium-containing active materials underlines the importance of dedicated in-depth future studies.

4. Conclusion

The addition of phosphoric acid (PA) to the aqueous electrode slurry containing $Li_4Ti_5O_{12}$ (LTO) supresses the aluminum current collector corrosion and leads to a superior cycling performance of such electrodes in terms of de-/lithiation kinetics and cycling stability. These enable a very good rate capability of the utilized micrometer-sized LTO particles. Most interestingly, the phosphate anion plays a decisive role in reducing the amount of lithium in the liquid phase. The leached lithium is, in fact, "trapped" in the formed rod-shaped lithium (titanium) phosphate particles that are found in the pristine and cycled LTO electrodes. The precise impact of these additional phases formed during the electrode preparation remains to be fully understood. Nonetheless, this finding highlights the need to carefully adjust the electrode slurry composition when adding acids to the aqueous electrode slurry to suppress the aluminum corrosion. We may, thus, anticipate that the findings reported herein will contribute to the eventual transition to the water-based electrodes processing by improving the understanding of the interactions of the active material and electrode slurry's additives.

CRediT authorship contribution statement

Yun Xu: Conceptualization, Methodology, Investigation, Formal analysis, Writing – original draft, Writing – review & editing. **Angelo Mullaliu:** Investigation, Formal analysis, Writing – review & editing. **Shawn D. Lin:** Investigation, Formal analysis, Writing – review & editing. **Yanjiao Ma:** Investigation, Formal analysis, Writing – original draft. **Jakob Asenbauer:** Investigation, Formal analysis, Writing – review & editing. **Maider Zarrabeitia:** Investigation, Formal analysis, Writing – review & editing. **Stefano Passerini:** Resources, Writing – review & editing. **Dominic Bresser:** Methodology, Conceptualization, Resources, Supervision, Writing – original draft, Writing – review & editing.

Declaration of Competing Interest

The authors declare no conflict of interest.

Data Availability

Data will be made available on request.

Acknowledgments

The authors would like to thank Ms. Annika Schuer and Mr. Cheng Xu for their support with the characterization of the electrodes. Moreover, the authors would like to acknowledge the financial support from the German Federal Ministry of Education and Research (BMBF) within the ExcellBattUlm project (03XP0257D) and the Helmholtz Association. Additionally, Y.X. and Y.M. gratefully acknowledge financial support from the Chinese Scholarship Council (CSC). S.D.L. thanks the Ministry of Science and Technology, Taiwan, for the financial support for his research visit to HIU.

Supplementary materials

Supplementary material associated with this article can be found, in the online version, at doi:10.1016/j.electacta.2022.140970.

References

[1] M. Armand, P. Axmann, D. Bresser, M. Copley, K. Edström, C. Ekberg, D. Guyomard, B. Lestriez, P. Novák, M. Petranikova, W. Porcher, S. Trabesinger, M. Wohlfahrt-Mehrens, H. Zhang, Lithium-ion batteries – current state of the art and anticipated developments, J. Power Sources. 479 (2020), 228708, https://doi.org/10.1016/j.jpowsour.2020.228708.

[2] D. Bresser, E. Paillard, M. Copley, P. Bishop, M. Winter, S. Passerini, The importance of "going nano" for high power battery materials, J. Power Sources. 219 (2012) 217–222, https://doi.org/10.1016/j.jpowsour.2012.07.035.

[3] T. Nemeth, P. Schröer, M. Kuipers, D.U. Sauer, Lithium titanate oxide battery cells for high-power automotive applications – electro-thermal properties, aging behavior and cost considerations, J. Energy Storage. 31 (2020), 101656, https://doi.org/10.1016/j.est.2020.101656.

[4] M.M. Thackeray, K. Amine, $Li_4Ti_5O_{12}$ spinel anodes, Nat. Energy 6 (2021) 683, https://doi.org/10.1038/s41560-021-00829-2. –683.

[5] P. Cicconi, L. Postacchini, E. Pallotta, A. Monteriù, M. Prist, M. Bevilacqua, M. Germani, A life cycle costing of compacted lithium titanium oxide batteries for industrial applications, J. Power Sources 436 (2019), 226837, https://doi.org/10.1016/j.jpowsour.2019.226837.

[6] X. Han, M. Ouyang, L. Lu, J. Li, Cycle life of commercial lithium-ion batteries with lithium titanium oxide anodes in electric vehicles, Energies 7 (2014) 4895–4909, https://doi.org/10.3390/en7084895.

[7] K. Ariyoshi, T. Ino, Y. Yamada, Rate capability of carbon-free lithium titanium oxide electrodes related to formation of electronic conduction paths observed by color change, J. Power Sources 430 (2019) 150–156, https://doi.org/10.1016/j.jpowsour.2019.05.023.

[8] A. Kraytsberg, Y. Ein-Eli, Conveying advanced Li-ion battery materials into practice the impact of electrode slurry preparation skills, Adv. Energy Mater. 6 (2016), 1600655, https://doi.org/10.1002/aenm.201600655.

[9] D. Bresser, D. Buchholz, A. Moretti, A. Varzi, S. Passerini, Alternative binders for sustainable electrochemical energy storage -the transition to aqueous electrode processing and bio-derived polymers, Energy Environ. Sci. 11 (2018) 3096–3127, https://doi.org/10.1039/C8EE00640G.

[10] Y. Qi, M.H.T. Nguyen, E.S. Oh, Enhancement of the lithium titanium oxide anode performance by the copolymerization of conductive polypyrrole with poly (acrylonitrile/butyl acrylate) binder, J. Appl. Electrochem. 50 (2020) 431–438, https://doi.org/10.1007/s10800-020-01401-8.

[11] B.R. Lee, E.S. Oh, Effect of molecular weight and degree of substitution of a sodium-carboxymethyl cellulose binder on $Li_4Ti_5O_{12}$ anodic performance, J. Phys. Chem. C 117 (2013) 4404–4409, https://doi.org/10.1021/jp311678p.

[12] S. Karuppiah, S. Franger, K. Nallathamby, Water-soluble green binder for $Li_4Ti_5O_{12}$ anodes: effect of binder choice on lithium storage, ChemElectroChem 5 (2018) 343–349, https://doi.org/10.1002/celc.201700963.

[13] V.D. Carvalho, N. Loeffler, G.-.T. Kim, M. Marinaro, M. Wohlfahrt-Mehrens, S. Passerini, Study of water-based lithium titanate electrode processing: the role of pH and binder molecular structure, Polymers 8 (2016), https://doi.org/10.3390/polym8080276. Basel.

[14] B.R. Lee, S. Kim, E.S. Oh, Bio-derivative galactomannan gum binders for $Li_4Ti_5O_{12}$ negative electrodes in lithium-ion batteries, J. Electrochem. Soc. 161 (2014) A2128–A2132, https://doi.org/10.1149/2.0641414jes.

[15] C. Fongy, P. Moreau, S. Chazelle, M. Bouvier, S. Jouanneau, D. Guyomard, B. Lestriez, Toward the aqueous processing of $Li_4Ti_5O_{12}$: a comparative study with $LiFePO_4$, J. Electrochem. Soc. 159 (2012) A1083, https://doi.org/10.1149/2.075207jes.

[16] R. Sahore, D.L. Wood, A. Kukay, K.M. Grady, J. Li, I. Belharouak, Towards understanding of cracking during drying of thick aqueous-processed $LiNi_{0.8}Mn_{0.1}Co_{0.1}O_2$ cathodes, ACS sustain, Chem. Eng. 8 (2020) 3162–3169, https://doi.org/10.1021/acssuschemeng.9b06363.

[17] W.B. Hawley, H.M. Meyer, J. Li, Enabling aqueous processing for $LiNi_{0.80}Co_{0.15}Al_{0.05}O_2$ (NCA)-based lithium-ion battery cathodes using polyacrylic acid, Electrochim. Acta 380 (2021), 138203, https://doi.org/10.1016/j.electacta.2021.138203.

[18] M. Wood, J. Li, R.E. Ruther, Z. Du, E.C. Self, H.M. Meyer, C. Daniel, I. Belharouak, D.L. Wood, Chemical stability and long-term cell performance of low-cobalt, Ni-Rich cathodes prepared by aqueous processing for high-energy Li-Ion batteries, Energy Storage Mater. 24 (2020) 188–197, https://doi.org/10.1016/j.ensm.2019.08.020.

[19] N. Loeffler, G.T. Kim, F. Mueller, T. Diemant, J.K. Kim, R.J. Behm, S. Passerini, *In situ* coating of $Li[Ni_{0.33}Mn_{0.33}Co_{0.33}]O_2$ particles to enable aqueous electrode processing, ChemSusChem 9 (2016) 1112–1117, https://doi.org/10.1002/cssc.201600353.

[20] M. Bichon, D. Sotta, N. Dupré, E. De Vito, A. Boulineau, W. Porcher, B. Lestriez, Study of immersion of $LiNi_{0.5}Mn_{0.3}Co_{0.2}O_2$ material in water for aqueous processing of positive electrode for Li-ion batteries, ACS Appl. Mater. Interfaces 11 (2019) 18331–18341, https://doi.org/10.1021/acsami.9b00999.

[21] A. Kukay, R. Sahore, A. Parejiya, W. Blake Hawley, J. Li, D.L. Wood, Aqueous Ni-rich-cathode dispersions processed with phosphoric acid for lithium-ion batteries with ultra-thick electrodes, J. Colloid Interface Sci. 581 (2021) 635–643, https://doi.org/10.1016/j.jcis.2020.07.144.

[22] M. Kuenzel, D. Bresser, T. Diemant, D.V. Carvalho, G.T. Kim, R.J. Behm, S. Passerini, Complementary strategies toward the aqueous processing of high-voltage $LiNi_{0.5}Mn_{1.5}O_4$ lithium-ion cathodes, ChemSusChem 11 (2018) 562–573, https://doi.org/10.1002/cssc.201702021.

[23] M. Kuenzel, D. Bresser, G.T. Kim, P. Axmann, M. Wohlfahrt-Mehrens, S. Passerini, Unveiling and amplifying the benefits of carbon-coated aluminum current collectors for sustainable $LiNi_{0.5}Mn_{1.5}O_4$ cathodes, ACS Appl. Energy Mater. 3 (2020) 218–230, https://doi.org/10.1021/acsaem.9b01302.

[24] M. Kuenzel, R. Porhiel, D. Bresser, J. Asenbauer, P. Axmann, M. Wohlfahrt-Mehrens, S. Passerini, Deriving structure-performance relations of chemically modified chitosan binders for sustainable high-voltage $LiNi_{0.5}Mn_{1.5}O_4$ cathodes, Batter. Supercaps. 3 (2020) 155–164, https://doi.org/10.1002/batt.201900140.

[25] M. Kuenzel, H. Choi, F. Wu, A. Kazzazi, P. Axmann, M. Wohlfahrt-Mehrens, D. Bresser, S. Passerini, Co-crosslinked water-soluble biopolymers as a binder for high-voltage $LiNi_{0.5}Mn_{1.5}O_4$|graphite lithium-ion full cells, ChemSusChem 13 (2020) 2650–2660, https://doi.org/10.1002/cssc.201903483.

[26] A. Kazzazi, D. Bresser, A. Birrozzi, J. von Zamory, M. Hekmatfar, S. Passerini, Comparative analysis of aqueous binders for high-energy Li-rich NMC as a lithium-ion cathode and the impact of adding phosphoric acid, ACS Appl. Mater. Interfaces 10 (2018) 17214–17222, https://doi.org/10.1021/acsami.8b03657.

[27] B.H. Toby, R.B. Von Dreele, GSAS-II: the genesis of a modern open-source all purpose crystallography software package, J. Appl. Crystallogr. 46 (2013) 544–549, https://doi.org/10.1107/S0021889813003531.

[28] K. Momma, F. Izumi, VESTA 3 for three-dimensional visualization of crystal, volumetric and morphology data, J. Appl. Crystallogr. 44 (2011), https://doi.org/10.1107/s0021889811038970.

[29] N. Jovic, B. Antic, A. Kremenovic, A. Spasojevic-De Bire, V. Spasojevic, Cation ordering and order-disorder phase transition in co-substituted $Li_4Ti_5O_{12}$ spinels, Phys. Status Solidi Appl. Res. 198 (2003) 18–28, https://doi.org/10.1002/pssa.200306451.

[30] X. Hao, B.M. Bartlett, $Li_4Ti_5O_{12}$ nanocrystals synthesized by carbon templating from solution precursors yield high performance thin film Li-ion battery electrodes, Adv. Energy Mater. 3 (2013) 753–761, https://doi.org/10.1002/aenm.201200964.

[31] T. Ohzuku, A. Ueda, N. Yamamoto, Zero-strain insertion material of $Li[Li_{1/3}Ti_{5/3}]O_4$ for rechargeable lithium cells, J. Electrochem. Soc. 142 (1995) 1431–1435, https://doi.org/10.1149/1.2048592.

[32] K. Ariyoshi, R. Yamato, T. Ohzuku, Zero-strain insertion mechanism of $Li[Li_{1/3}Ti_{5/3}]O$ for advanced lithium-ion (shuttlecock) batteries, Electrochim. Acta 51 (2005) 1125–1129, https://doi.org/10.1016/j.electacta.2005.05.053.

[33] B. Xue, K. Wang, Y. Tan, Q. Li, J. Sun, Fabrication and performance of $Li_4Ti_5O_{12}$/cotton-driven carbon fiber as anode for lithium-ion batteries, Ionics 25 (2019) 2535–2542, https://doi.org/10.1007/s11581-018-2738-5. Kiel.

[34] W.B. Hawley, A. Parejiya, Y. Bai, H.M. Meyer, D.L. Wood, J. Li, Lithium and transition metal dissolution due to aqueous processing in lithium-ion battery cathode active materials, J. Power Sources 466 (2020), 228315, https://doi.org/10.1016/j.jpowsour.2020.228315.

[35] L. Azhari, X. Zhou, B. Sousa, Z. Yang, G. Gao, Y. Wang, Effects of extended aqueous processing on structure, chemistry, and performance of polycrystalline $LiNixMnyCozO_2$ cathode powders, ACS Appl. Mater. Interfaces 12 (2020) 57963–57974, https://doi.org/10.1021/acsami.0c20105.

[36] S.Y. Li, B.C. Church, Effect of aqueous-based cathode slurry pH and immersion time on corrosion of aluminum current collector in lithium-ion batteries, Mater. Corros. 67 (2016) 978–987, https://doi.org/10.1002/maco.201608843.

[37] J.F. Moulder, Handbook of X-Ray Photoelectron Spectroscopy: A Reference Book of Standard Spectra for Identification and Interpretation of XPS Data, Physical Electronics Division Perkin-Elmer Corporation, 1992.

[38] R. Franke, T. Chassé, P. Streubel, A. Meisel, Auger parameters and relaxation energies of phosphorus in solid compounds, J. Electron Spectrosc. Relat. Phenom. 56 (1991) 381–388, https://doi.org/10.1016/0368-2048(91)85035-R.

[39] N.V. Kosova, D.I. Osintsev, N.F. Uvarov, E.T. Devyatkina, Lithium titanium phosphate as cathode, anode and electrolyte for lithium rechargeable batteries, Chem. Sustain. Dev. 13 (2005) 253–260.

[40] Y. Kee, N. Dimov, K. Minami, S. Okada, Orthorhombic lithium titanium phosphate as an anode material for Li-ion rechargeable battery, Electrochim. Acta 174 (2015) 516–520, https://doi.org/10.1016/j.electacta.2015.06.032.

[41] Z. Liu, X. Qin, H. Xu, G. Chen, One-pot synthesis of carbon-coated nanosized $LiTi_2(PO_4)_3$ as anode materials for aqueous lithium ion batteries, J. Power Sources 293 (2015) 562–569, https://doi.org/10.1016/j.jpowsour.2015.05.092.

[42] N.D. Luchinin, D.A. Aksyonov, A.V. Morozov, S.V. Ryazantsev, V.A. Nikitina, A. A. Abakumov, E.V. Antipov, S.S. Fedotov, α-$TiPO_4$ as a negative electrode material for lithium-ion batteries, Inorg. Chem. 60 (2021) 12237–12246.

[43] H. Miyashiro, S. Seki, Y. Kobayashi, Y. Ohno, Y. Mita, A. Usami, All-solid-state lithium polymer secondary battery with $LiNi_{0.5}Mn_{1.5}O_4$ by mixing of Li_3PO_4, Electrochem. Commun. 7 (2005) 1083–1086, https://doi.org/10.1016/j.elecom.2005.08.006.

[44] S. Wu, J.J. Shiu, J.Y. Lin, Effects of Fe_2P and Li_3PO_4 additives on the cycling performance of $LiFePO_4$/C composite cathode materials, J. Power Sources 196 (2011) 6676–6681, https://doi.org/10.1016/j.jpowsour.2010.11.138.

[45] Y. Sun, L. Zan, Y. Zhang, Effects of Li_3PO_4 additive on the electrochemical properties of Li_2FeSiO_4 as cathode material for lithium-ion batteries, J. Mater. Sci. Mater. Electron. 30 (2019) 15582–15591, https://doi.org/10.1007/s10854-019-01934-5.

[46] C.F. Sun, J. Hu, P. Wang, X.Y. Cheng, S.B. Lee, Y. Wang, Li_3PO_4 matrix enables a long cycle life and high energy efficiency bismuth-based battery, Nano Lett. 16 (2016) 5875–5882, https://doi.org/10.1021/acs.nanolett.6b02720.

[47] M. Cabello, G.F. Ortiz, M.C. López, P. Lavela, R. Alcántara, J.L. Tirado, Self-assembled $Li_4Ti_5O_{12}/TiO_2/Li_3PO_4$ for integrated Li–ion microbatteries, Electrochem. Commun. 56 (2015) 61–64, https://doi.org/10.1016/j.elecom.2015.04.011.